AN SH0 LITHIUM NIOBATE DISPERSIVE DELAY LINE FOR CHIRP COMPRESSION-ENABLED LOW POWER RADIOS

Tomás Manzaneque, Ruochen Lu, Yansong Yang and Songbin Gong
University of Illinois at Urbana-Champaign, Urbana, USA

ABSTRACT

This paper presents the first demonstration of a shear-horizontal mode Lithium Niobate dispersive delay line, featuring a center frequency of 250 MHz, a delay-bandwidth (*TB*) product of 100, an electromechanical coupling (k^2) in excess of 35%, and a low insertion loss of 10 dB. The high compression is attained via a large bandwidth of 125 MHz, centered at 250 MHz, and an extensive delay of 0.8 μS. The device shown herein has greatly outperformed the state of the art, namely surface acoustic wave delay lines which typically have an insertion loss over 25 dB for a comparable compression ratio. The attained performance can be attributed to the excellent piezoelectric coupling of lamb waves in a suspended Lithium Niobate X-cut thin film. A voltage gain of 3 has been demonstrated for instantaneously amplifying chirp-coded signals, a feature that can be harnessed to enhance signal to noise ratio in low power wake-up radios for Internet of Things (IoT) applications.

INTRODUCTION

Internet of Things (IoT) has been identified as the next technology revolution that will reshape our societies. As IoT starts to promise many exciting applications, one of the most fundamental challenges of IoT, namely wireless connectivity at extremely low power, remains under-addressed. Having access to radio frequency (RF) transceivers operating with near zero power and high sensitivity would significantly prolong the operation of battery-powered "things" and lower the cost of sustaining the IoT infrastructure. Unfortunately, as of late 2016, near zero/low power radios remain a technology bottleneck with the SoA low power radios consuming ~100nWs of power and featuring limited functionality [1], [2].

To drastically reduce the power consumption, one viable approach is to keep the wireless connection dormant when no functionality is required and enable it upon the detection of an incoming wakeup signal. Given that power consumption in stand-by state of the radio is small or near zero in comparison to the active state, this approach is effective for reducing the power consumed for IoT connectivity as many "things" operate with significant latency between active periods. Note that the near zero stand by power for the radio receiver has to be achieved while maintaining a very high sensitivity for detecting faint wake-up signals so that the burden of lower receiver power is not shifted to transmitting higher power signals.

Fig. 1 shows a promising method to implement a chirp-enabled low-power wakeup radio. In this notional scheme, the wake-up signal takes the form of pulses coded with linear chirps, which are fed to a receiver composed of a chain of chirp compressor, rectifier, comparator and correlator. The chirp compressor turns the input signal to magnitude-amplified and duration-shorten signals that can

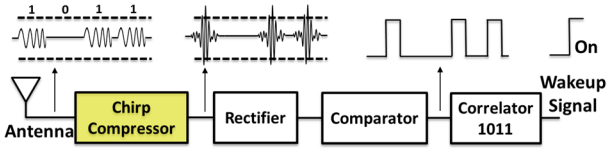

Figure 1: Notional scheme for a chirp-enabled wakeup radio. The chirp compressor provides passive voltage gain and enhanced SNR to improve the sensitivity.

overcome the high threshold voltage of the follow-on semiconductor or MEMS rectifier [3], [4]. The envelop-detection via the rectifier and digitization by the follow-on comparator then convert the signal into a code string bearing the wake-up signature. If the code matches the wakeup sequence programmed in the correlator, a wakeup pulse is produced to turn on the full communication capabilities of the IoT device for the active periods.

The chirp-coded wake up radio relies on the passive chirp compressor to provide high processing gain so that voltages of the wakeup signal are amplified and the signal to noise ratio (*SNR*) is improved concurrently [5]. Thus, the passive chirp compressor plays a key role in overcoming the major challenge of attaining high sensitivity and consuming no power at the same time. The SoA passive chirp compression at RF typically resorts to surface acoustic waves (SAW) dispersive delay structures [6]. However, it has not been possible to attain voltage gain with SAW devices due to their high insertion loss (*IL*) caused by scattering and narrow chirp bandwidth limited by the electromechanical coupling (k^2) and impedance matching. Recently, lamb wave modes (e.g. SH0 and S0) have been demonstrated with high k^2 and low loss in suspended single crystal Lithium Niobate ($LiNbO_3$) thin films enabled by film transfer techniques [7], [8], [9]. The high k^2 (>25%) for these modes is enabled by pronounced piezoelectricity in single crystal $LiNbO_3$, while the thin film structure confines the acoustic propagation and eliminates the electrode-induced scattering into the substrate. Leveraging the high coupling and low loss, we design and implement a chirp compressor based on the shear-horizontal (SH0) mode in an X-cut $LiNbO_3$ thin film. The fabricated device demonstrates a very low *IL* of 10 dB, a fractional bandwidth (*FBW*) of 50%, a differential delay of 0.8 μs, and a voltage gain of 3, thanks to an electromechanical coupling in excess of 35% and low wave propagation loss. The performance widely surpasses that of $LiNbO_3$ SAW devices, which typically have *IL* > 25 dB for a comparable compression ratio, resulting in a voltage gain much less than unity [6].

THEORY AND DESIGN

As seen in Fig. 2(a), the SH0 dispersive delay line is formed by two identical and symmetrically arranged interdigital transducers (IDTs) oriented -10° to -Y axis on a suspended X-cut $LiNbO_3$ thin film. The pitch of both IDTs varies linearly in the longitudinal direction from W_{max} to W_{min}, defining the transducer (or chirp) bandwidth as:

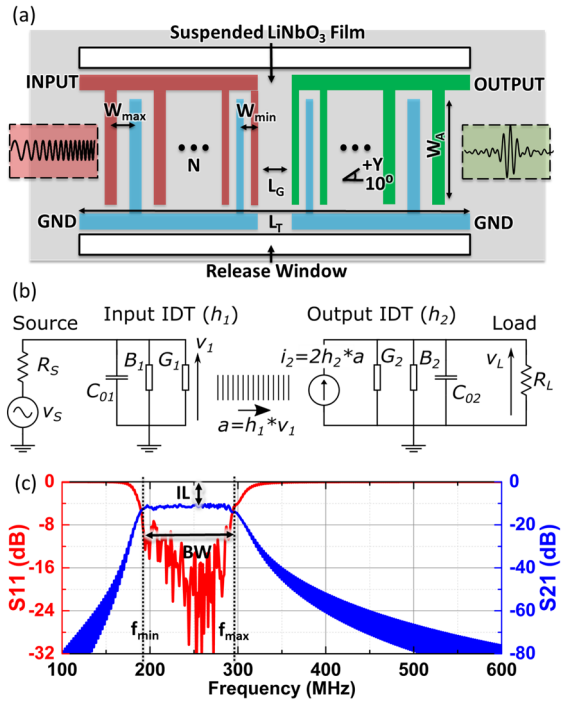

Figure 2: (a) Top view of the $LiNbO_3$ chirp compressor. (b) Electrical model of an acoustic delay line. (c) S-parameters obtained from the model for the design in Table 1.

$$B = f_{max} - f_{min} = \frac{v_p}{2}\left(\frac{1}{W_{min}} - \frac{1}{W_{max}}\right), \qquad (1)$$

where v_p is the phase velocity of SH0 acoustic waves, and f is frequency at which the transduction for IDT of a pitch W is maximum.

Applying a signal linearly chirped from f_{min} to f_{max} over a period T to the input IDT would produce acoustic waves that are eventually sensed by the output IDT after they propagate across the film. Due to the spatial variation of the IDT pitch, the lowest frequency signal (f_{min}) in the chirp, excited by the electrode pair of W_{max} on the far end, would travel a longer distance (L_T) than the highest frequency signal, which only transverse a distance of L_G. The spatial variation in IDT essentially produces a delay dependent on frequency and dispersive by engineering. Given that the duration of the chirp (T) is set to satisfy:

$$T = \frac{L_T - L_G}{v_p}, \qquad (2)$$

all the frequencies in chirp would coincide in time at the output port, constructively increasing the instantaneous power by TB.

To model the chirp compressor response analytically in both the frequency and time domains, we employ the model reported in [10], with which the input and output transducers are defined by their impulse response $h_1(t)$ and $h_2(t)$ (i.e. the acoustic wave generated by an impulse input signal v_1). The impulse response can be approximated by:

$$h(t) = 4\sqrt{k^2 C_s f_i^3(t)}\, sin\left(2\pi \int_0^t f_i(\tau)d\tau\right), \qquad (3)$$

where C_s is the static capacitance per electrode pair, and $f_i(t)$ is the center frequency of the transducer at a distance of tv_p from the IDT edge in the center section of the delay line. The duration of the impulse response, or time delay, is then given by T. It is worth noting that C_s and k^2 are both dependent on the ratio of the electrode pitch to the film thickness, which varies across the IDTs. The current generated at the output IDT can be obtained by correlation as:

$$i_2(t) = 2 \cdot h_1(t) * h_2(t) * v_1(t), \qquad (4)$$

if the propagation loss is neglected. The maximum compression can be achieved if the combined impulse response of both IDTs matches the time reverse of the input voltage:

$$h_{12}(t) = h_1(t) * h_2(t) = c_0 v_1(t_0 - t); \qquad (5)$$

$i_2(t)$ is then the delayed autocorrelation function of $v_1(t)$. Using energy conservation, it can be shown that the instantaneous power over the duration (1/B) of the compressed signal is magnified by a factor of TB [6]. Note that the compression is not applied to the noise as it is not correlated to $h_{12}(t)$. Consequently, the SNR is enhanced approximately by TB [6].

Assume that the average values of C_s and k^2 for the spatially varying IDTs can be used as approximations, a lumped element model seen in Fig. 2(b) can be constructed for representing the electrical behavior of the chirp compressor. G and B represent the acoustic conductance and susceptance, respectively. The former can be deduced from energy conservation as:

$$G(\omega) = 2|H(\omega)|^2, \qquad (6)$$

where $H(\omega)$ is the Fourier transform of $h(t)$, and B is the Hilbert transform of G. The factor of 2 in Eq. 6 arises from the bi-directionality of the IDT. It implies that the power is radiated to or harnessed from both lateral directions equally. For a bidirectional design such as the one in Fig. 3(a), 3/4 of the energy is not captured by the output and is lost to surroundings. Therefore, the minimum insertion loss (IL) of the delay line is 6 dB.

Impedance mismatch at ports will also add to the IL. Matching the IDTs impedance to the source and load impedances is essential to optimize the performance. To do so, the transducers have to be designed with:

$$G_1(\omega_0) = \frac{1}{R_S} \qquad G_2(\omega_0) = \frac{1}{R_L}, \qquad (8)$$

where R_S and R_L are respectively the source and load impedances, and ω_0 is the center frequency of the delay line. In addition to setting G_1 and G_2, shunt inductors are required at both ports to tune out the port capacitances C_{01} and C_{02} at ω_0. The acoustic susceptances are neglected in

Table 1: Design parameters of the chirp compressor.

Symbol	Description	Value
L_T	Total length	3.1 mm
W_A	Acoustic aperture	0.2 mm
L_G	Gap length	0.1 mm
W_{min}	Minimum pitch	6 μm
W_{max}	Maximum pitch	10 μm
N	# of electrode pairs / IDT	100
TB	Compression ratio	100
B/f_0	Fractional bandwidth	50%

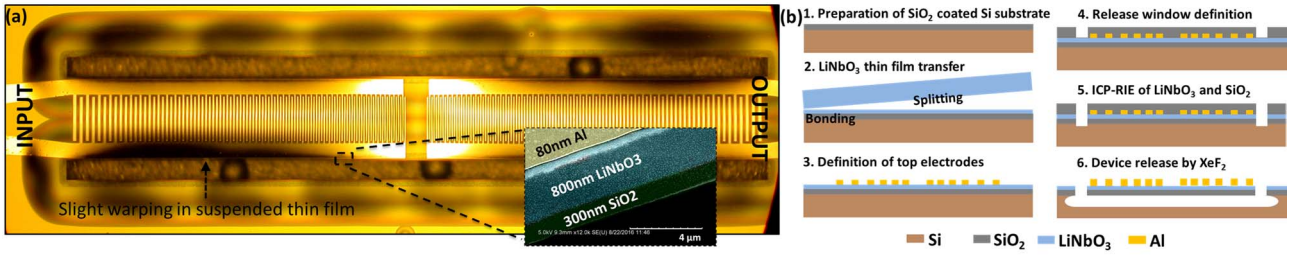

Figure 3: (a) Optical microscope image of the fabricated chirp compressor with zoomed-in view of the etched film stack. (b) Flow graph of the fabrication process.

impedance matching because they are typically insignificant relative to G and C_0. Note that ideal matching cannot be attained uniformly over the entire chirp bandwidth as the acoustic conductance varies with frequency. Moreover, inductive matching is only effective over a given *FBW*, of which the maximum is set by [6], [10]:

$$\left(\frac{B}{f_0}\right)_{max} = \sqrt{\frac{4k^2}{\pi}}. \tag{9}$$

Note that k^2 imposes the ultimate limit for the *FBW*.

Besides the bi-directionality of the transducers and port mismatch, wave propagation loss in the $LiNbO_3$ thin film and ohmic dissipation in the metal lines and electrodes can also increase *IL*. The overall *IL*, in combination with *TB*, determines the voltage at the output. It can be shown that the voltage gain, defined as the maximum amplitude of the compressed wave at the output divided by the amplitude of the input wave, is given by:

$$g_v = \sqrt{\frac{TB}{10^{IL/10}} \cdot \frac{R_L}{R_S}}. \tag{10}$$

Guided by the aforementioned model, a chirp compressor is designed with the parameters listed in Table I to provide a compression ratio/processing gain of 100. The parameters are named in accordance with labels in Fig. 2(a). Note that although the bandwidth (Eq. 1) and time delay (Eq. 2) are dependent on the phase velocity, both the compression ratio (*TB*) and fractional bandwidth can be solely determined by physical dimensions:

$$TB = \frac{L_T - L_G}{2}\left(\frac{1}{W_{min}} - \frac{1}{W_{max}}\right), \tag{11}$$

$$\frac{B}{f_0} = 2\left(\frac{W_{max} - W_{min}}{W_{max} + W_{min}}\right). \tag{12}$$

The S-parameter performance can also be predicted for this design, using the model in Fig. 2(b) and assuming $k^2 = 39\%$ and 4 dB loss to account for the propagation and other parasitic effects. The simulated response of the designed delay line with 150 Ω terminations and inductive matching is plotted in Fig. 2(c). Given that the return loss has been minimized in the simulation, the *IL* seen is mostly the result of the bi-directionality (6 dB) and the assumed 4 dB loss from attenuation and parasitic effects.

FABRICATION AND MEASUREMENTS

The device was fabricated using a process depicted in Fig. 3(b). The process starts with the ion-slicing based film transfer process to attain single crystal X-cut $LiNbO_3$ thin film on a carrier with an intermediate layer of SiO_2 [9]. In

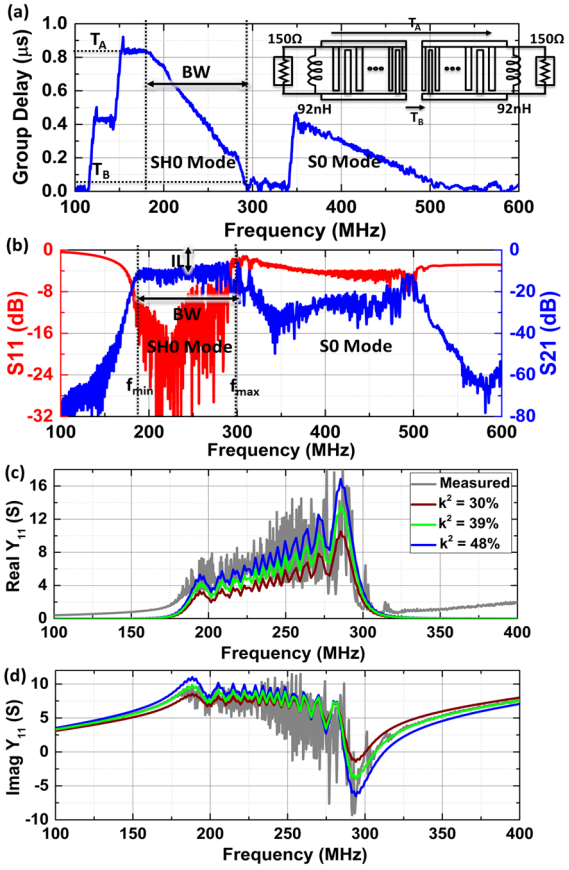

Figure 4: Measured (a) group delay and (b) S-parameters over a wide frequency range. Measured and calculated (c) conductance and (d) susceptance for different k^2.

this case, a high resistivity Si wafer was used as the carrier. The IDT electrodes are then defined by the liftoff of an 80nm sputtered Al. A PECVD SiO_2 layer is deposited and patterned with reactive ion etching (RIE) to serve as the hard mask for etching $LiNbO_3$. Next, Cl_2-based RIE with inductively coupled plasma (ICP) is used to etch the $LiNbO_3$ thin film. Upon its completion, the top SiO_2 mask is completely removed by RIE. As the last step, the device is released by removing the Si underneath the delay line with XeF_2-based isotropic etching. The fabricated chirp compressor is shown in Fig. 3(a) with the stack of layers shown in the inset. Despite the large length-to-thickness ratio of the delay line structure, only regional warping is observed and the delay line is fully suspended without cracking the thin film. The SiO_2 underneath the $LiNbO_3$ was used to facilitate film transfer and is left in place to provide temperature compensation to the chirp compressor.

To validate the performance, frequency domain characterizations of the fabricated device were first done with

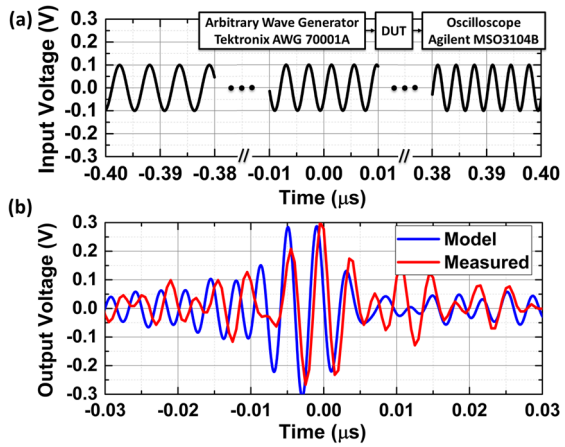

Figure 5: (a) Input chirp signal. (b) Measured output voltage compared with the result simulated with k^2 = 39% and 3 dB loss extrinsic to the bi-directionality of the IDTs.

S-parameter measurements, from which the measured group delay from the input to output is found and shown in Fig. 4(a). The total achieved differential time delay is 0.8 μs between signals at f_{min} and f_{max}, which corresponds to a phase velocity of 3750 m/s for the SH0 mode (Eq. 2). The phase velocity sets the f_{min} and f_{max} to be 187 and 312 MHz, suggesting a center frequency and bandwidth of 250 and 125 MHz, respectively. Additional dispersive response is observed at higher frequencies (350-500 MHz), due to the inadvertent S0 mode excitation.

As seen in Fig. 4(b), the measured *IL* has an average of about 10 dB when 92 nH ($Q = 50$) inductors are used to impedance match the ports of 150 Ω. The return loss is better than 12 dB in the BW. From the *IL*, the loss extrinsic to bi-directionality is estimated to average at 3 dB and maximize at 5 dB at the lower frequencies.

In order to estimate the k^2 of the transducers, the Y_{11} was simulated for various k^2 values and compared with the measured Y_{11}. The simulation of Y_{11} was done with the lumped element model (Fig. 2(b)) and a C_s value extracted from the measurement. To extract the C_s, the total capacitance of the transducer was first calculated from the imaginary part of the measured Y_{11} at a frequency far from the acoustic emission bands of S0 and SH0 modes, and was then averaged over the number of transducer pairs. The obtained value for C_s is 38 fF. The comparison between the simulated and measured Y_{11} is shown in Fig. 4(c) and (d). It is challenging to precisely determine the k^2 due to the large ripples in the measured data. Nonetheless, an estimate of 39% for k^2 can be concluded from the comparison. The estimation is also on par with the k^2 value predicted by a FEM simulation of the $LiNbO_3/SiO_2$ stack. Based on Eq. 9, the large k^2 permits an even greater *FBW* (up to 70%) than the demonstrated 50% for the chirp compressor without compromising the *IL* due to impedance mismatch.

Time-domain measurements were also carried out to validate the chirp compression without inductive matching at ports. A Tektronix AWG 70001A with $R_S = 50\ \Omega$ was employed to generate the input chirp when the response at the output was recorded with an Agilent MSO3104B oscilloscope (input impedance set to 1 MΩ). As shown in Fig. 5, for an input chirp of 100 mV in amplitude, an amplification of 3 has been achieved. This result is compared with simulated results in the time domain. The simulation also used the lumped element model and assumed k^2 = 39% and a constant 3 dB loss extrinsic to the IDT bi-directionality over the entire bandwidth. Calculations based on the fabricated device reveal that a higher gain of 5 can be attained by including 92 nH inductors in parallel with the 50 Ω input and 1MΩ output terminations.

CONCLUSIONS

An SH0 $LiNbO_3$ chirp compressor has been demonstrated for the first time with a differential delay of 0.8 μs, a *BW* of 125 MHz, a *TB* product of 100, and an average *IL* of 10 dB. The device has been validated to provide not only large processing gain and *SNR* enhancement, but also a voltage gain of 3. The high performance has been accomplished thanks to the high electromechanical coupling coefficient of SH0 waves and the acoustic confinement in a suspended X-cut $LiNbO_3$ thin film. Based on this platform, higher compression ratios and voltage gains can be envisioned provided future improvement and design optimization can enable a larger *TB* and lower *IL*. Most importantly, this new class of devices brings new possibilities for low power wakeup radio receivers, a key enabling technology for the Internet of Things.

ACKNOWLEDGEMENTS

The authors thank the DARPA NZERO program for funding support, and Dr. Troy Olsson for valuable discussions.

REFERENCES

[1] M. Magno and L. Benini. "An ultra low power high sensitivity wake-up radio receiver with addressing capability." In 2014 IEEE 10th International Conference on Wireless and Mobile Computing, Networking and Communications (WiMob), pp. 92-99. 2014.

[2] N. E. Roberts and D. D. Wentzloff. "A 98nW wake-up radio for wireless body area networks." In 2012 IEEE Radio Frequency Integrated Circuits Symposium, pp. 373-376. 2012.

[3] D. A. Czaplewski, et al. "A nanomechanical switch for integration with CMOS logic." Journal of Micromechanics and Microengineering 19, no. 8 (2009): 085003

[4] J-O. Lee, Y-H. Song, M-W Kim, M-H. Kang, J-S. Oh, H-H. Yang, and J-B. Yoon. "A sub-1-volt nanoelectromechanical switching device." Nature nanotechnology 8, no. 1 (2013): 36-40.

[5] J. R. Klauder, et al. "The theory and design of chirp radars." *Bell System Technical Journal* 39.4 (1960): 745-808.

[6] D. Morgan, "Surface Acoustic Wave Filters," Elsevier, 2007.

[7] S. Gong, and G. Piazza. "Design and analysis of lithium–niobate-based high electromechanical coupling RF-MEMS resonators for wideband filtering." *IEEE Transactions on Microwave Theory and Techniques*61, no. 1 (2013): 403-414.

[8] R. H. Olsson et al. "A high electromechanical coupling coefficient SH0 Lamb wave lithium niobate micromechanical resonator and a method for fabrication." *Sensors and Actuators A: Physical* 209 (2014): 183-190.

[9] Y-H. Song and S. Gong. "Elimination of spurious modes in SH0 lithium niobate laterally vibrating resonators." *IEEE Electron Device Letters*36, no. 11 (2015): 1198-1201.

[10] C. S. Hartmann, D. T. Bell, and R. C. Rosenfeld. "Impulse model design of acoustic surface-wave filters." *IEEE Transactions on Microwave Theory and Techniques* 21, no. 4 (1973): 162-175.